Tensile behavior of $Al_{1-x}Mo_x$ crystalline and amorphous thin films

D.S. Gianola [a,*], Z. Lee [b,c], C. Ophus [b,d], E.J. Luber [d], D. Mitlin [d], U. Dahmen [b],
K.J. Hemker [e], V.R. Radmilović [b,f,*]

[a] *Department of Materials Science and Engineering, University of Pennsylvania, Philadelphia, PA, USA*
[b] *National Center for Electron Microscopy, Lawrence Berkeley National Laboratory, University of California, Berkeley, CA, USA*
[c] *School of Mechanical and Advanced Materials Engineering, Ulsan National Institute of Science and Technology, Ulsan, Republic of Korea*
[d] *Department of Materials and Chemical Engineering, University of Alberta, Edmonton, Alberta, Canada*
[e] *Department of Mechanical Engineering and Materials Science and Engineering Johns Hopkins University, Baltimore, MD, USA*
[f] *University of Belgrade, Faculty of Technology and Metallurgy, Nanotechnology and Functional Materials Center, Belgrade, Serbia*

Abstract

The exceptional strength and distinct deformation physics exhibited by pure ultrafine-grained and nanocrystalline metals in comparison to their microcrystalline counterparts have been ascribed to the dominant influence of grain boundaries in accommodating plastic flow. Such grain-boundary-mediated mechanisms can be augmented by additional strengthening in nanocrystalline alloys via solute and precipitate interactions with dislocations, although its potency is a function of the changes in the elastic properties of the alloyed material. In this study, we investigate the elastic and plastic properties of $Al_{1-x}Mo_x$ alloys ($0 \leqslant x \leqslant 0.32$) by tensile testing of sputter-deposited freestanding thin films. Isotropic elastic constants and strength are measured over the composition range for which three microstructural regimes are identified, including solid solutions, face-centered cubic and amorphous phase mixtures and body-centered cubic (bcc)/amorphous mixtures. Whereas the bulk modulus is measured to follow the rule of mixtures over the Mo composition range, the Young's and shear moduli do not. Poisson's ratio is non-monotonic with increasing Mo content, showing a discontinuous change at the onset of the bcc/amorphous two-phase region. The strengthening measured in alloyed thin films can be adequately predicted in the solid solution regime only by combining solute strengthening with a grain boundary pinning model. The single-step co-sputtering procedure presented here results in diversity of alloy compositions and microstructures, offering a promising avenue for tailoring the mechanical behavior of thin films.
© 2012 Acta Materialia Inc. Published by Elsevier Ltd. All rights reserved.

Keywords: Thin films; MEMS/NEMS; Amorphous metals; Nanocrystalline metals; Elastic properties

1. Introduction

Polycrystalline metals consisting of grains with sizes less than 500 nm (ultrafine-grained) and smaller (less than 100 nm, nanocrystalline) have received considerable

research and industrial attention in recent years, owing to their impressive strengths in comparison to their coarse-grained counterparts. Central to the mechanical property enhancements that have piqued interest in these materials for structural applications, including yield strength [1–4], fatigue resistance [5–8] and wear resistance [9–11], are transitions in the underlying deformation mechanisms that accommodate plastic flow as the grain size enters the sub-micron regime and approaches the nanometer scale [12–29]. Following extensive fundamental investigations into these novel plasticity mechanisms over the last decade or so (e.g. see thorough reviews on this topic in Refs. [3,4,30]), the emerging picture is that the strength- and

---

* Corresponding authors. Addresses: Department of Materials Science and Engineering, University of Pennsylvania, Philadelphia, USA. Tel.: +1 215 898 7974 (D.S. Gianola), University of Belgrade, Faculty of Technology and Metallurgy, Belgrade, Serbia. Tel.: +381 11 3370 469 (V.R. Radmilović).

E-mail addresses: gianola@seas.upenn.edu (D.S. Gianola), VRRadmilovic@tmf.bg.ac.rs, VRRadmilovic@lbl.gov (V.R. Radmilović).

rate-limiting processes occur at, and are controlled by, the large volume fraction of interfacial material residing at grain boundaries (GBs). As the mean free path required for conventional dislocation–dislocation interactions and subsequent plasticity mechanisms such as dislocation forest (i.e. Taylor) hardening becomes large relative to the grain size and new mechanisms become energetically favorable, including partial dislocation emission and absorption [17,31,32], deformation twinning [13,33,34], GB sliding [20,35,36] and GB migration [37–40]. Much of the evolution in the understanding of the active mechanisms has been the result of experimental studies of nominally pure nanocrystalline metals and informed via atomistic simulations of pure materials.

However, truly pure nanocrystalline metals are known to be thermodynamically unstable [41], and thus the thermal stability displayed by most of these materials suggests that some amount of impurities is present to energetically stabilize GBs [42–45] or kinetically hinder microstructural evolution [46–48]. Indeed, solute atoms within a nanocrystalline solvent have been shown to segregate to GBs and increase stability. Additional driving forces such as stress have also been shown to catalyze grain growth or refinement [27,39,49–54], and recent studies have identified minute concentrations of impurities at GBs as potent stabilizers against such evolution [55–58]. The need to understand the role of additional elements incorporated into nanocrystalline metals is underscored by the additional enhancements that can be achieved in multi-component systems where alloying effects augment the new deformation mechanisms. Despite the promise of alloying, relatively little attention has been given to studying such nanocrystalline metals, in part due to the difficulty of deconvoluting the effects of grain size and chemistry [59]. As alloying can cause changes to both elastic and plastic properties, an experimental approach capable of independently measuring the full suite of mechanical properties is requisite to predictive capability.

In parallel to these fundamental studies, metallic thin films employed in applications such as integrated circuits, micro- and nanoelectromechanical systems (MEMS/NEMS) energy storage and energy conversion, where good electrical conductivity is demanded in dimensionally constrained systems, are often deposited or grown in nanostructured forms using far-from-equilibrium approaches (e.g. vapor deposition, electrodeposition, etc.). As the dimensions of features comprising these devices are reduced to nanometer scales, the appropriate geometric and surface roughness requirements become harder to achieve using standard film synthesis and microfabrication methods. This is primarily because the size of the internal microstructure of these thin film materials is of the order of the feature itself; the nature of crystalline growth during thin film synthesis can preclude having smooth, conformally coating material [60]. Recently, Lee and colleagues fabricated NEMS cantilever structures fashioned from Al–Mo sputtered thin films, which were compositionally opti-mized for mechanical properties and roughness [61,62]. These authors found the optimum composition for the use as NEMS resonators to be Al–32 at.% Mo, which exhibited a composite structure consisting of an amorphous Al matrix and dispersed Mo nanocrystallites. This material displayed low roughness ($r_{rms} < 5$ nm), high hardness ($H > 5$ GPa) and high stiffness as deduced from nanoindentation (reduced modulus, $E_r \sim 150$ GPa). These results are promising for NEMS applications, but the full constitutive behavior of this material is still unknown, precluding rational design and device lifetime prediction.

In this paper, we report on the uniaxial tensile response of Al–Mo submicron freestanding thin films across a wide compositional range resulting in both crystalline and amorphous phases to elucidate the role of alloying on elastic and fracture behavior in ultrafine grained and nanocrystalline metals. We chose the Al–Mo binary system [63] as a model material to gain fundamental insight into the role of alloying additions on mechanical behavior of thin films; moreover, Al–Mo alloys and multilayers [64–67] have also been proposed as a good candidate material for corrosion-resistant coatings [68–71].

2. Materials and methods

$Al_{1-x}Mo_x$ films of compositions ranging from pure Al to Al–32 at.% Mo (0, 2, 4, 8, 16, 24 and 32 at.% Mo) were deposited onto laboratory-grade naturally oxidized 4 inch silicon $\langle 100 \rangle$ wafers by DC magnetron co-sputtering from pure Mo and pure Al targets. Wafers were either cleaned with a 3:1 mixture of 51% H_2SO_4 and 30% H_2O_2 or etched with HF prior to deposition. The argon sputtering pressure was 7.0 mTorr following evacuation to a vacuum base pressure of 1×10^{-6} Torr. Film depositions were performed with substrate rotation during deposition to ensure film uniformity. The Al sputtering rate was kept constant at 10.5 nm min^{-1} (300 W power) while the Mo sputtering rate was adjusted to create the desired composition. All films had a thickness of $\sim$200 nm. X-ray photoelectron spectroscopy was used to verify the global thin film composition as well as to determine the contamination levels. The only detectable impurity was oxygen, which was present at a maximum value of 4 at.%. Microstructural characterization was performed using transmission electron microscopy (TEM) of freestanding films, which are electron-transparent in the as-deposited state. Cross-sectional TEM samples were prepared according to the procedure outlined in Refs. [61,62]. Lattice parameters were determined using X-ray diffraction (XRD) operated in standard powder diffraction geometry. XRD profiles indicated strong $\langle 111 \rangle$ and $\langle 110 \rangle$ film textures for the face-centered cubic (fcc) and body centered cubic (bcc) phases, respectively, beyond film compositions of 4 at.% Mo. Atomic force microscope (AFM) operated in tapping mode was employed to characterize surface roughness and measure surface grain sizes.

Pre-fabricated Si-based testing frames (1×1 cm) were introduced in the vacuum chamber during deposition to

create thin film tensile specimens. Thin film mechanical behavior was determined using a custom-built microtensile specimen testing apparatus. Details regarding the mechanical testing setup and microfabrication of the specimen testing frames can be found in Refs. [27,54,72,73]. Local two-dimensional full-field strains were calculated using an in-house digital image correlation (DIC) code [73–76], which, combined with force measurement, allowed for the evaluation of a full suite of material properties including strength, ductility, elastic moduli and Poisson's ratio (defined as the absolute value of the ratio of transverse to axial strains in the elastic regime). In brief, intensity profiles of hundreds of fine silica particles deposited on the surface of the films are fit with a nonlinear least squares routine and tracked during deformation. Subsequent calculation of displacements and strain quantities is performed from the particle positions. This strain measurement approach offers sufficient resolution ($\sim$30 and 50 $\mu\varepsilon$ in the longitudinal and transverse directions, respectively) to measure small elastic strains. All tensile experiments were conducted at a constant strain rate of $\sim10^{-5}\,\text{s}^{-1}$. Mechanical properties extracted from tensile measurements were compared to nanoindentation results from nominally identical films across the composition range, as reported in Ref. [61]. Nanoindentation was performed using a commercially available load–depth sensing instrument (Hysitron Tribo-Indenter), equipped with an AFM. A Berkovich indenter tip was used, with a target indentation depth of 150 nm. The presented hardness and modulus values are each calculated as the average from 25 individual indentations, each separated by $\sim$25 μm.

3. Structural and chemical characterization

The morphology of the Al–Mo films was examined using TEM. Fig. 1 shows representative bright field TEM images of four different Al–Mo compositions in plan view. The pure Al film in Fig. 1a has large crystalline grains, with the largest having diameters on the order of several times the film thickness. A grain size distribution for the pure Al films was calculated from over 400 measurements from plan view TEM images and is given in Fig. 2, which shows a mean grain size of 370 ± 199 nm. Gaps between a portion of the grains can be seen, demonstrating significant porosity present in the film. Addition of 8 at.% Mo shows a microstructure with finer Al fcc grains (150 ± 42 nm). The microstructure also is somewhat porous, though with a much finer pore structure than that of the pure Al. Fig. 1c shows the structure of the thin film with 16 at.% Mo. This composition's morphology is further refined, consisting of a mixture of nanoscale crystalline and amorphous regions with no evident porosity. Further alloying additions are shown for the 32 at.% Mo composition in Fig. 1d. This alloy is primarily composed of amorphous material, with a fine network of O-rich and Mo-depleted bands a few nanometers thick (determined by nano-probe electron energy loss spectroscopy). To determine the effect of Mo content on mean grain size over the entire composition range, AFM was used to characterize the surface of thicker films ($t = 1.5\,\mu$m) and surface grain diameters were measured. Fig. 3 shows that the mean grain size decreases with increasing Mo content, consistent with other reports of grain size stabilization in Al thin films [55,58]. Despite the difference in film thickness for the AFM data plotted in Fig. 3 in comparison to the films employed for tensile testing, the mean grain sizes for the pure (370 and 387 nm for thin and thick films, respectively) and 8 at.% Mo (150 and 164 nm for thin and thick films, respectively) films show good agreement, suggesting that the Mo content is the predominant factor in controlling the microstructure rather than the film geometry.

To further elucidate the morphology of the Al–Mo compositions exhibiting very fine microstructure, we performed high-resolution transmission electron microscopy (HRTEM) of selected thin films. Fig. 4a shows a HRTEM micrograph of the $Al_{84}Mo_{16}$ film in cross-section. The structure is composed of nanoscale fcc crystallites embedded in a continuous amorphous matrix. Fourier transforms of the HRTEM images confirm such a two-phase microstructure via evidence of both discrete crystalline spots and a diffuse halo characteristic of amorphous materials. The microstructure of the $Al_{68}Mo_{32}$ film is shown in Fig. 4b, which is primarily amorphous with small amounts of ordered bcc domains. We note that XRD patterns for the compositional range of $\sim$20 and 45 at.% Mo showed no visible crystalline peaks, suggesting a completely amorphous compositional regime. However, the ordered domains evident in HRTEM images obtained from films within this compositional regime would be expected to contribute very weakly to the scattered X-ray intensity. Thus, we hereafter refer to this regime as two-phase. Taken as a whole, we can roughly identify three regimes over the composition range studied here: (i) fcc solid solution, (ii) fcc and amorphous two-phase material and (iii) bcc and amorphous two-phase material. To determine the compositional limit of the fcc solid solution regime, we performed XRD of thin films and calculated lattice parameters based on the measured Bragg peak positions of the fcc Al phase. Fig. 5 shows the lattice parameter a as a function of Mo composition, with the error bars representing the standard deviation of a from the fitted peaks. At the pure Al extreme, the lattice parameter was measured to be very close to the known $a_{Al} = 4.048$ Å. The data up to $\sim$10 at.% Mo shows a linear decrease in a, illustrating Vegard's law and the accommodation of Mo solute atoms in Al. In this regime, we can describe the lattice parameter changes with composition as $a = a_{Al} + kc$, where c is the Mo atomic fraction and k is a proportionality constant equal to -0.36 Å for our alloyed thin films. However, at compositions above 10 at.% Mo, the fcc lattice parameter saturates with increasing alloying content, suggesting that additional Mo is incorporated into the amorphous phase. As the lattice parameters measured in XRD correspond to the grain interiors where diffraction occurs [77,78], it is
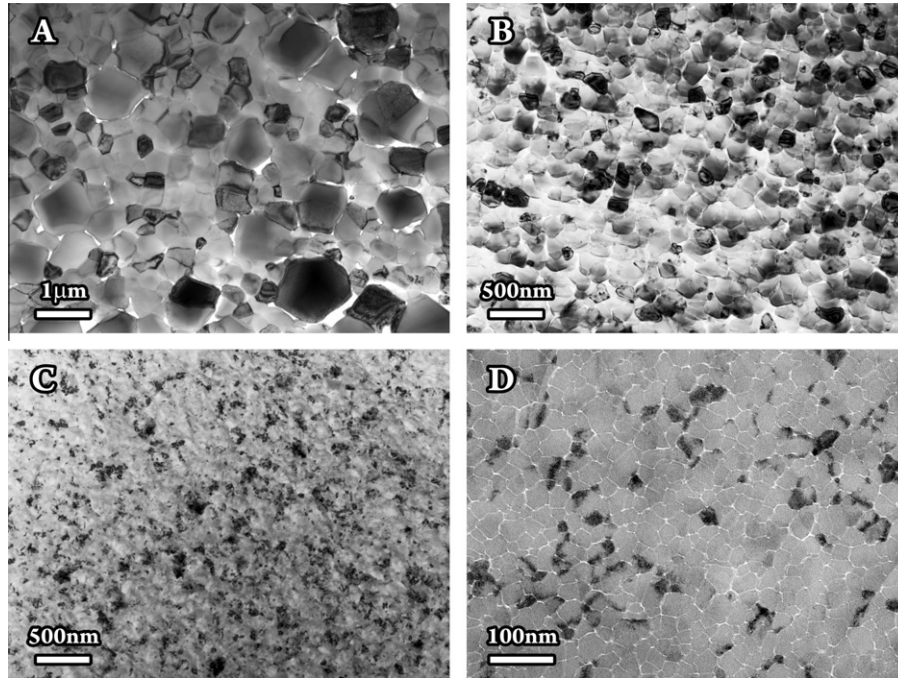
Fig. 1. Plan view bright field TEM micrographs of (a) pure Al, (b) $Al_{0.92}Mo_{0.08}$, (c) $Al_{0.84}Mo_{0.16}$ and (d) $Al_{0.68}Mo_{0.32}$ thin films. Note different scale bars.
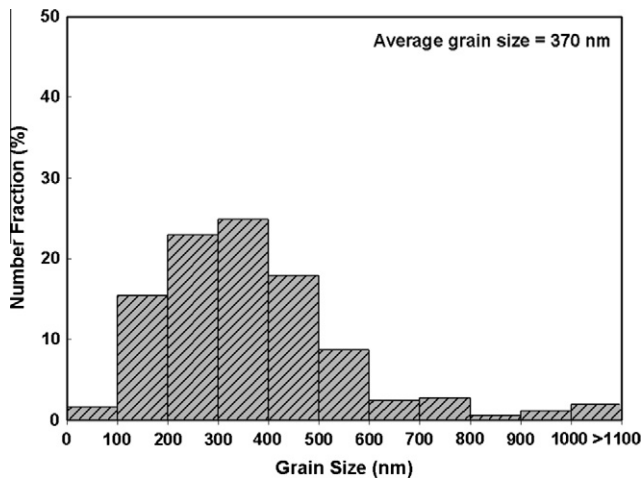

Fig. 2. Histogram of grain size in as-deposited pure Al film.

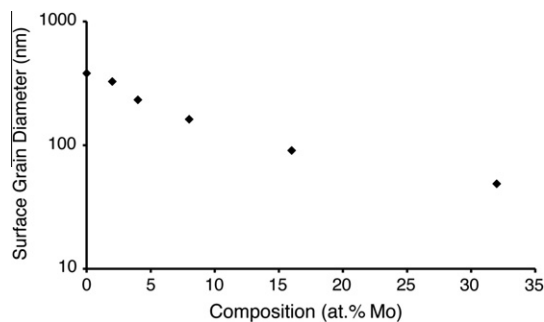Fig. 3. Surface grain diameter obtained by AFM of thicker films ($t = 1.5$ μm).

possible that Mo segregates to grain boundaries as well. Nevertheless, the fcc phase in our thin films is capable of dissolving large solute quantities, well in excess of the equilibrium solubility of Mo in Al [79]. Since the amorphous phase is evident in films with compositions larger than 10 at.% Mo, and the fcc phase disappears above ~20 at.% Mo (interpolating between measured compositions), we can assume that 20 at.% Mo is roughly the composition of the amorphous phase at this limit. This allows us to estimate the volume fraction of the amorphous phase (assuming a linear rule of mixtures) to be ~2/3 at a composition of 16 at.% Mo, as shown in Fig. 4a.

4. Mechanical behavior of thin films

4.1. Elastic response

Representative tensile stress–strain curves illustrating the mechanical behavior of Al–Mo thin films as a function of Mo content are shown in Fig. 6. The alloyed films all exhibited strong and brittle response, in contrast to the behavior of the pure Al films, which exhibited plastic strains in excess of 15%. Differences in the Young's modulus appear to systematically correlate with the composition of the film, with larger Mo content showing higher moduli. The Young's moduli of all alloyed films were markedly higher than the pure Al film, which was measured from unloads to avoid contributions from microplasticity. Beginning with the pure film, Young's modulus was measured to be lower than that of bulk Al, likely due to the presence of some porosity in the thin films at levels low enough (estimated to be between 1–2% as measured by TEM and SEM images) to afford the material with
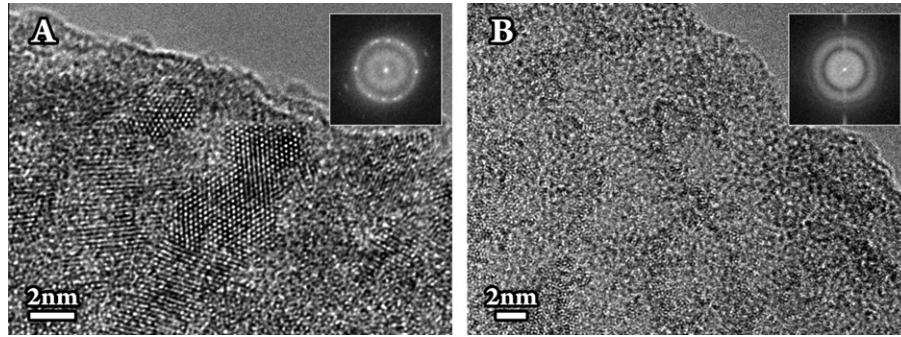
Fig. 4. HRTEM micrographs of (A) $Al_{0.84}Mo_{0.16}$ and (B) $Al_{0.68}Mo_{0.32}$ thin films in cross-section. Insets give FFTs, confirming presence of nanocrystallites within an amorphous matrix in $Al_{0.84}Mo_{0.16}$ and a fully amorphous $Al_{0.68}Mo_{0.32}$. It should be noted that small amounts of ordered bcc domains were found in the $Al_{0.68}Mo_{0.32}$ sample.
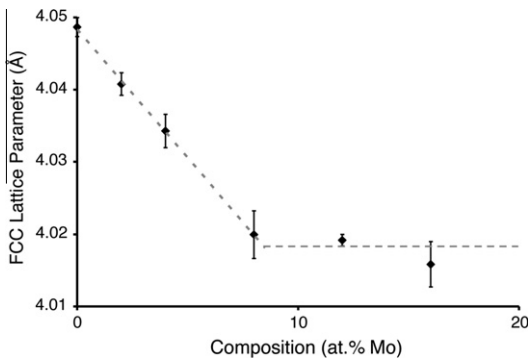

Fig. 5. fcc Lattice parameter as a function of Mo content. The error bars show the standard deviation of the measured lattice parameters from the fitted peaks.
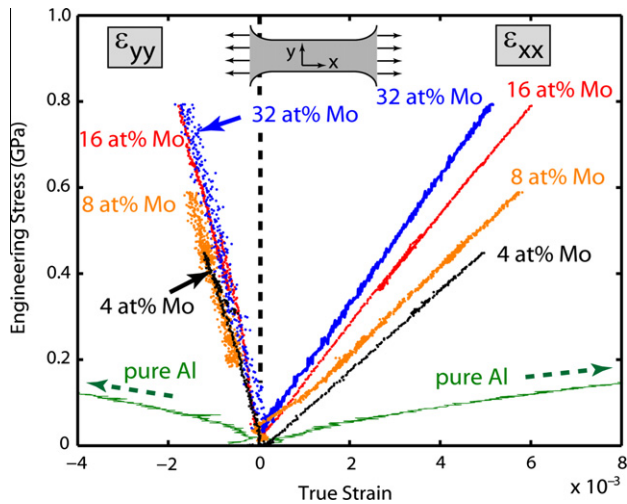

Fig. 6. Representative tensile response for films with varying Mo content. The stress–strain curves are plotted for both the longitudinal (ε_{xx}) and transverse (ε_{yy}) directions, which allowed for the measurement of Poisson's ratio. The full curve for a pure Al film has been truncated to highlight the differences between alloy films.

Poisson contraction. The negative ratio of the transverse to axial strains gives the Poisson's ratio ($v = -\varepsilon_{yy}/\varepsilon_{xx}$), which was computed for all alloy compositions.

The isotropic elastic constants (Young's modulus and Poisson's ratio) of the Al–Mo films are shown as a function of Mo content in Fig. 7a and b, respectively. The standard isotropic elastic relations:
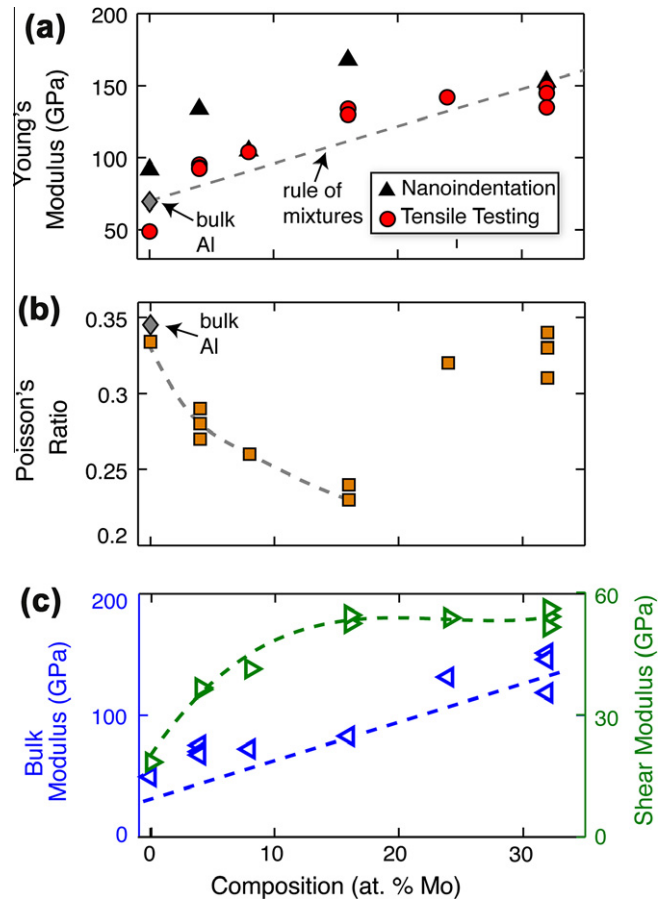

Fig. 7. Measured elastic constants as a function of at.% Mo and tensile testing of freestanding thin films: (a) Young's modulus, (b) Poisson's ratio and (c) bulk and shear moduli calculated assuming elastic isotropy. The reduced modulus of the films on Si substrates as measured by nanoindentation [61] are also shown for comparison.

substantial ductility. The relatively large width of the thin film tensile samples (600 μm specimen widths) coupled with the use of DIC methods enabled direct measurement of transverse strains (ε_{yy}) during tensile loading, which are also plotted in Fig. 6 and have negative values owing to

$$G = \frac{E}{2(1+v)}; \quad B = \frac{E}{3(1-2v)} \quad (1)$$

were used to calculate the bulk (B) and shear (G) moduli as plotted in Fig. 7c. Young's, bulk and shear moduli are seen to increase with increasing addition of the stiffer Mo atom. However, the trends with increasing alloying content are nonlinear with the exception of the bulk modulus, in contrast to the prediction of a simple rule of mixtures relationship based on the moduli of pure Al (70 GPa) and Mo (329 GPa). Both the Young's and shear moduli appear to saturate above ~20 at.% Mo at values of ~150 and 50 GPa, respectively.

Interestingly, Poisson's ratio was measured to be non-monotonic over the studied compositional range, decreasing with increasing Mo content to values as low as 0.23. However, films with concentrations higher than 20 at.% Mo show an apparent discontinuous jump to values similar to those of pure Al (0.35) and Mo (0.38). Whereas the onset of the amorphous phase does not measurably change the trend in Poisson's ratio with increasing Mo content, the sharp increase in Poisson's ratio of the film correlates with the presence of small ordered bcc domains.

4.2. Fracture strength

Fracture strengths of these films also were measured to strongly depend on the alloy composition with the general trend of higher strength with increasing addition of Mo. The stress–strain behavior and ultimate tensile strength of the pure Al thin films were found to agree very well with other reports of sputter-deposited Al films synthesized under similar conditions [27,28,39,55]. The relatively large ductility measured in similar pure Al nanocrystalline films tested in tension was shown to be a result of stress-driven grain growth. This phenomenon was reported [27,29] to have a dramatic and dynamic effect on the mechanical response, in particular the ductility of these films. In addition, the impurity content at grain boundaries was shown to control the propensity for stress-driven microstructural evolution [55,58], suggesting that that the pure films studied here possessed low impurity concentrations.

The addition of Mo in the alloyed thin films clearly strengthens the material, as demonstrated in Fig. 8. The fcc solid solution compositional range demonstrates the most potent strengthening, while the strength appears to saturate at compositions higher than 18 at.% Mo. To investigate the influence of stress state, our tensile data are compared to hardness values obtained from nanoindenation of thicker films (1.5 μm) with the same nominal composition [61]. The strengthening and hardening trends were measured to correlate linearly, as shown in the inset of Fig. 8, suggesting a similar mechanism responsible for strengthening over this compositional range. However, the slope of tensile strength vs. hardness gives a value much larger than the standard Tabor relation of $H = 3\sigma$. Proportionality constants different from 3 have been previously
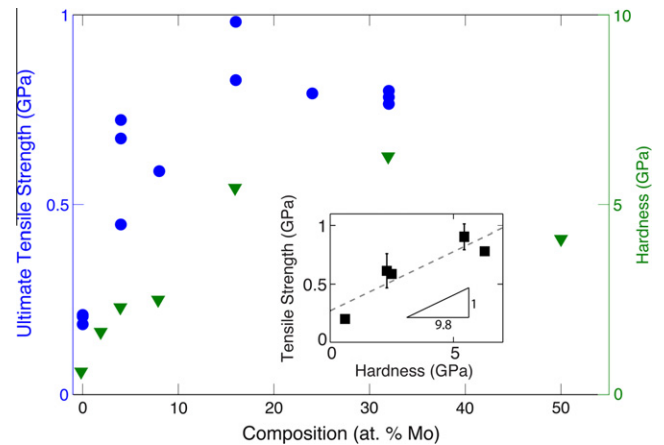

Fig. 8. Ultimate strength (obtained from tensile testing) and hardness (obtained from nanoindentation) as a function of Mo composition. The inset shows a linear relationship between tensile strength and hardness, with a slope below that of the Tabor relationship $\sigma = $ H3.

measured in nanocrystalline metals [21], ceramics [80] and metallic glasses [81–83] and have been attributed to the pressure dependence of plastic yielding in materials that undergo shear-induced dilations or transformation plasticity. Such mechanisms in our two-phase amorphous regimes could be active, but the large ratio between hardness and tensile strength values could also be enhanced by film porosity, leading to premature fracture in tension.

In summary, both the elastic constants and tensile strength depend strongly on the Mo content and generally do not follow a simple rule-of-mixtures relationship. In the subsequent discussion, we analyze these results in the context of the different microstructures that develop over our studied compositional range and propose mechanistic insight to our measured trends.

5. Discussion

5.1. Elastic properties

Our results show the following trends in elastic constants with increasing Mo content: (i) Young's modulus (E) increases in a nonlinear manner with the largest changes occurring in dilute solutions, followed by an apparent saturation (~150 GPa, nearly 2× higher than the pure Al thin films) at the highest concentrations studied, (ii) bulk modulus (B) shows a linear increase that is well captured by a rule of mixtures model, (iii) shear modulus (G) shows a similar trend to that of Young's modulus, and increases by a factor of 3 over that of the pure Al thin films and (iv) Poisson's ratio decreases nonlinearly in the solid solution and two-phase fcc/amorphous regimes, followed by a discontinuous increase at Mo content larger than 20 at.%. The large changes in E in the solid solution regime amount to 10% per 1% of Mo added, larger than what has been reported for bulk Al–Mo alloys (3% increase for every 1% of Mo) [84].

Given the thin film geometry and corresponding microstructure that evolves as a result of the sputtering process, it is worth considering the role of elastic anisotropy in our tensile measurements. The direct measurements of Young's modulus and Poisson's ratio are based on in-plane quantities, which for a $\langle 111 \rangle$ textured film with cubic symmetry are isotropic. Use of Eq. (1) to calculate shear and bulk moduli assume full isotropy of the film, which could be influenced by the measured texture in the thin films. However, the elastic anisotropy ratios of both Al and Mo, defined as $AR = 2C_{44}/(C_{11} - C_{12})$ where C_{ij} represent the components of the elastic stiffness tensor, are 1.22 and 0.91, respectively, representing low elastic anisotropy ($AR = 1$ for a perfectly isotropic material). Thus, we conclude that our assumption of isotropy for calculation of the shear and bulk moduli is reasonable and would not substantially influence accurate measurement of the full suite of elastic properties.

Comparison of our experimental results with trends in elastic constants of other Al–M alloys serves as a useful guide for understanding the origins of our measured changes. Table 1 gives properties and corresponding elasticity trends for several different solute elements added to an Al solvent, as obtained via experimental measurements and ab initio calculations [85–87]. One general trend that emerges is the strong correlation that exists between increases in bulk and Young's moduli and decreasing lattice parameter upon incorporation of solute atoms, sug-

gesting that bond stiffening occurs when the solute reduces the atomic volume of the alloy [88]. This is also true of our Al–Mo thin film alloys, despite the atomic size of Mo being larger than that of Al. Such a phenomenon has also been observed in Al–Cu alloys, which (like Mo) introduces monovalent solute into a trivalent Al matrix, has a larger atomic radius, is a stiffer element ($E_{Cu} = 120$ GPa, $B_{Cu} = 140$ GPa), and results in decreases in the lattice parameter of the alloy relative to pure Al. That Cu additions to Al only cause subtle increases to elastic constants [86,89], while Mo additions produce substantial increases as we have measured ($\sim$3 GPa per at.% Mo), suggests that the drastic stiffness contrast between pure Mo ($E_{Mo} = 329$ GPa, $B_{Mo} = 230$ GPa) and Al controls the magnitude of stiffening. The correlation between elastic constants and lattice parameter leads to a linear increase of the bulk modulus with increasing solute content (Fig. 7c), which can be reconciled by the adherence of our lattice parameter data to Vegard's law (Fig. 5) and considering that bulk modulus represents the elastic stiffness in a hydrostatic stress state [90].

While the Young's and shear moduli also show increases with increasing Mo content, we have measured their relationships to be nonlinear (Fig. 7). This behavior is likely a result of changes in the local atomic environment upon incorporation of Mo solute atoms, changing the electronic structure and thus the elastic constants that represent non-hydrostatic stress states. Indeed, classic Zener theory [91]

Table 1
Elastic properties and trends in binary Al–M solid solution alloys, including current study of $Al_{1-x}Mo_x$ thin films.

Element	Xtal	r (pm)	Val. e^-	E_{solute} (GPa)	G_{solute} (GPa)	B_{solute} (GPa)	v_{solute}	A***	E_{Al-M}	G_{Al-M}	B_{Al-M}	$(a_o)_{Al-M}$	G/B_{Al-M}
Al[a]	fcc	118	3	70	26	76	.35	.08					
Li[b]	bcc	145	1	5	4	11	.43	1.43	↑	↑	↓		↑
Li[c]	bcc	145	1	5	4	11	.43	1.43	↑	↑	↑	↓	
Be[c]	hcp	112	2	287	132	130	.03	-.1	↑		↑	↓	
Cu[c]	fcc	145	1	120	48	140	.34	.64	↑		↑	↓	
Na[c]	bcc	190	1	10	3	6	.24	.96			↓	↑	
Mg[c]	hcp	145	2	45	17	45	.29	-.01	↓		↓	↑	
Ca[c]	fcc	194	2	20	7	17	.31		↓		↓	↑	
Si[d]	diam	111	4	150	80	100	.26	.35	↓	↓	↑		↓
Ge[d]	diam	125	4	103	41	71	.26	.41	↓	↓		↑	
Mo[†]	bcc	190	1	329	126	230	.31	-.2	↑*	↑*	↑**	↓	↑

Quantities highlighted in blue and red indicate a property that is lower or higher than that of the pure Al solvent, respectively.
[a] Ref. [110].
[b] Ref. [85].
[c] Ref. [86].
[d] Ref. [87].
[e] Current study of Al–Mo thin films.
[*] Does not follow rule of mixtures.
[**] Follows rule of mixtures.
[***] Anisotropy ratio defined as $(2C_{44} + C_{12})/(C_{11} - 1)$ and $C_{33}/(C_{11} - 1)$ in cubic and hcp crystals, respectively, with $A = 0$ being perfectly isotropic.

predicts changes to the shear modulus to be predominately a result of the internal strain ε_a in a solid solution, as expressed by

$$\frac{1}{G}\left(\frac{\partial G}{\partial c}\right) = \frac{4\varepsilon_a^2}{k_B N}\left(\frac{\partial G}{\partial T}\right) \tag{2}$$

where $\varepsilon_a = (1/a)(\partial a/\partial c)$, N is the number density of atoms, and $\partial G/\partial T$ gives the temperature dependence of the shear modulus of pure Al. Our measurements of a in the solid solution regime give ε_a as constant (Fig. 5), and $\partial G/\partial T$ can be represented as constant near room temperature [87]. Eq. (2) would consequently predict a linear dependence of G with increasing Mo solute content, in contrast to our measurements of G. Thus, it is reasonable to conclude that additional factors other than internal strain, such as charge transfer and changes to the electronic structure, must be considered to account for changes in G in our Al–Mo alloys. Changes to the Poisson's ratio upon alloying with Mo (Fig. 7b) are also likely affected by such factors. Beyond the solid solution regime, the sudden increase in Poisson's ratio is presumed to be a result of the accommodation of multi-axial strain by the amorphous/glassy composite or the emergence of ordered bcc domains in the two-phase material.

Our results showing substantial changes to all isotropic elastic constants also highlight the importance of the testing approach used for measuring thin film alloy properties. For instance, calculation of the Young's modulus from nanoindentation measurements requires either the assumption that the Poisson's ratio of the sample does not change with alloying [86] or independent measurement via alternate approaches. This interdependence of elastic constants is a result of the multiaxial stress state beneath the indenter tip and is demonstrated through the reduced modulus E_r measured in nanoindentation as given by:

$$\frac{1}{E_r} = \frac{1 - v_i^2}{E_i} + \frac{1 - v_s^2}{E_s} \tag{3}$$

where the subscripts i and s denote the indenter and specimen, respectively [92]. Measurements of the full isotropic elastic constants of Al–Mo alloy thin films via tensile testing allow us to more accurately determine properties extracted from nanoindentation results. Using our measured Poisson's ratio values (Fig. 7b) and E_r measured in a previous study of similar Al–Mo films [61], we calculated E_s to compare with Young's modulus measured from tensile tests, as shown in Fig. 7a. The trend of increasing modulus with increasing Mo content is identical, although the nanoindentation results were consistently higher than those from tensile testing. This result could be explained by several factors. First, the film thicknesses of the specimens used for nanoindentation were 1.5 μm [61], significantly thicker than those deposited for tensile testing (∼200 nm), which likely results in distinct mean grain sizes and grain size distributions (evidenced by different surface morphologies and roughness). As the elastic properties are generally considered to be microstructure-independent (for

the grain sizes obtained in this study), we hypothesize that levels and through-thickness variations in porosity could be different between the two batches of films, resulting in changes in apparent moduli. Nevertheless, determination of the compositional dependence of v is needed to accurately measure E_s in these alloy thin films.

5.2. Strengthening mechanisms

Several strength-controlling mechanisms could govern the behavior of our Al–Mo alloys depending on the composition of the thin film. Below ∼10 at.% Mo, the microstructure consists of an fcc solid solution with ultrafine grains, leading to solution-based and grain boundary strengthening. Above 10 at.% Mo, two-phase microstructures emerge with a significant amorphous content, in which distinct mechanisms are expected to control the strength of the material. We will treat these regimes separately to model the measured tensile strengths.

At low Mo compositions, classical solid solution strengthening theories that treat the interaction of dislocations with solute atoms that distort the lattice can be applied. One such theory is the well-known Fleischer model that readily applies to substitutional solutes in a cubic metal solvent [93,94]. According to Fleischer, the magnitude of strengthening $\Delta\tau_{SS}$ that occurs on the dislocation slip plane is proportional to the square root of composition c, as given by:

$$\Delta\tau_{SS} = \beta G_o \varepsilon_{SS}^{3/2} c^{1/2} \tag{4}$$

where β is a proportionality constant related to obstacle strength, G_o is the shear modulus of the solvent, and ε_{SS} is an interaction parameter that describes the changes to the lattice parameter and shear modulus of the solvent owing to the presence of the solute atoms. The interaction term expands as:

$$\varepsilon_{SS} = \left| \frac{\frac{1}{G_o}\frac{\partial G}{\partial c}}{1 + \frac{1}{2}\left|\frac{1}{G_o}\frac{\partial G}{\partial c}\right|} - \frac{3}{b_o}\frac{\partial b}{\partial c} \right| \tag{5}$$

where b_o is the Burgers vector of the solvent. The first and second terms in the brackets represent the influence of changes in stiffness and volume with alloying, respectively. We can directly estimate the predicted strengthening increment due to a solid solution since we have experimental measurements of shear moduli and lattice parameters as a function of composition. Fitting of the data in Fig. 5 in the solid solution regime yields $\partial b/\partial c = -0.36$ Å, while the shear modulus variation $\partial G/\partial c = 286$ GPa is given by the data in Fig. 7c. Using measurements for the pure Al solvent and a value of $\beta = 1/120$ (representative of bulk Al alloys [88]), we can calculate $\Delta\tau_{SS}$ to compare with our measured data as shown in Fig. 9. It is evident that solid solution strengthening alone describes the lower range of our data relatively well in the single-phase regime.

This model of strengthening alone, however, does not incorporate the effects of grain boundaries as obstacles to

dislocation motion. Rupert and colleagues recently developed a model for an additional strengthening term that accounts for the effects of solute in a nanocrystalline alloy that is governed by distinct deformation mechanisms from its microcrystalline counterpart [59]. Based on a comparison of nanocrystalline Ni–W sputtered and electrodeposited alloys, they were able to deconvolute the combined effects of mean grain size d and solute content and showed that their data could only be described by considering the additional role that solutes play when grain boundaries serve as pinning points for dislocation motion. This model assumes a scenario where a dislocation is nucleated at grain boundaries and bows across the grain whilst being pinned at either end by the grain boundaries, as has been suggested by several researchers [22,31,32,95,96]. This strengthening mechanism is thus grain size dependent, with the strengthening modeled as $\tau = Gb/d$ [31]. These authors argue that the effect of solutes in such a scenario can be incorporated via changes in G and b with atomic fraction of solute, analogous to the Fleischer model. Accordingly, they predict the shear strength of a nanocrystalline alloy as [59]:

$$\tau = \Delta\tau_{SS} + \frac{G_o b_o}{d}\left[1 + \left(\frac{1}{G_o}\frac{\partial G}{\partial c} + \frac{1}{b_o}\frac{\partial b}{\partial c}\right)\right] \tag{6}$$

Fitting the measurements of mean grain sizes for our Al–Mo alloys and using a Taylor factor of 3.06 for an fcc polycrystalline material with random grain orientations, we can substitute all values into Eq. (6) and compare with our measured tensile strengths. Fig. 9 shows the comparison of our data with the nanocrystalline solution pinning model (green curve calculated from the second term of Eq. (6)) [59] as well as the combined effects of Fleischer solid solution strengthening with nanocrystalline solution pinning (black curve). It is clear that the Fleischer contribution dominates in our Al–Mo alloys owing to the relatively large grain sizes we have in comparison with the Ni–W alloys [59]. Nevertheless, the model predicts strength in the range of our experimental data (note that the only fitting parameter not directly measured is β), which suggests that the additional terms coupling grain-boundary-mediated deformation mechanisms with the role of solutes could be needed for a complete description of strength.

Beyond the fcc solid solution regime (>10 at.% Mo), two-phase regions emerge, combining an amorphous phase with fcc (at intermediate compositions) and bcc phases (>25 at.% Mo). We measure tensile strengths in these two-phase regimes that are independent of the Mo content with magnitudes that are similar to those films at the limit of the solid solution regime. This suggests that the properties of the crystalline composite may control the strength, and the amorphous phase either: (a) has properties similar to its crystal counterpart and are weakly dependent on composition, or (b) introduces interfaces with strengths equal to or greater than the grain boundaries present in the crystal. We also note that the tensile strength of amorphous metals at low temperatures is well known to be closely proportional to G; often reported to be ~0.025G [81,108]. This is consistent with our measurements of our tensile strengths and G values that are roughly constant over the amorphous composite regime with a ratio of ~0.02G, suggesting that the properties of the amorphous material do not vary significantly with composition. Given the compositional flexibility in these regions, tailoring of length scales of the glassy/crystalline aggregate could be an interesting avenue of research. Indeed, glassy/crystalline metallic composites have been developed by other researchers in an attempt to achieve combinations of strength and tensile ductility [97–101], and typically rely on exploiting length scales in the glassy phase that are below the critical crack length for fracture [81,99,102–104].

5.3. Potential for tensile ductility through alloy design

It has been shown that ratio of the shear modulus G to the bulk modulus B, can be a good phenomenological indicator of the ability to exhibit ductility, both in crystalline [105,106] and metallic glass materials [81,107–109]. For example, ductile fcc metals have a low G/B ratio, while brittle bcc metals give a high G/B [105,106]. In an amorphous material, this can be rationalized by considering a glass that strongly resembles an incompressible fluid ($v = 0.5$) with capacity for easy flow in shear. Schroers and Johnson reported significant ductility in $Pt_{57.5}Cu_{14.7}Ni_{5.3}P_{22.5}$ bulk metallic glass ($G/B = 0.17$) and attributed the unusual deformation behavior to the suppression of unstable cracks leading to multiple shear band formation, owing to the high Poisson's ratio of the material (thus, a high G/B ratio). It is therefore evident that utilizing a metallic glass with a high Poisson's ratio is one approach for increasing the intrinsic ductility of a material that is otherwise brittle.

Fig. 10 shows G/B for the Al–Mo alloyed films studied here, where the shear and bulk moduli are calculated from elastic properties determined directly from tension testing, in comparison to values for several pure metals. Below 10
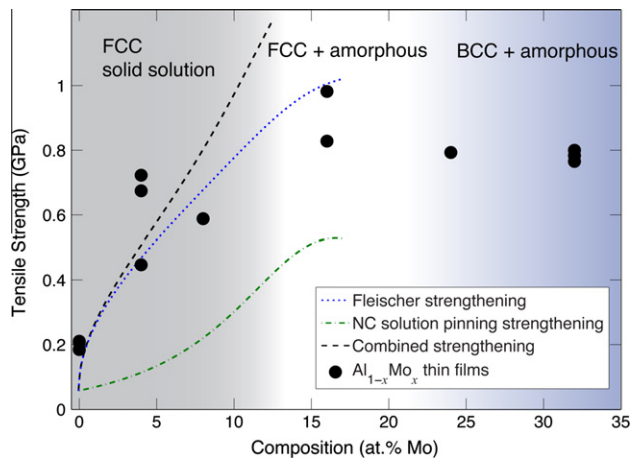
Fig. 9. Comparison of measured tensile strengths of $Al_{1-x}Mo_x$ thin films with strengthening theories. Models shown include solid solution strengthening (blue curve), nanocrystalline pinning strengthening (green curve) and a combination of both (black curve). (For interpretation of the references to colour in this figure legend, the reader is referred to the web version of this article.)

at.% Mo, where the material remains fully crystalline, G/B increases from ∼0.38 to 0.57, suggesting that solid solutioning may impart intrinsically brittle behavior. In the two-phase fcc/amorphous region, G/B maintains its high value. However, the presence of the bcc ordered domains at higher Mo concentrations drastically reduces G/B to values close to that of Mo and for ductile pure metals (e.g. Cu). This framework suggests that the higher Mo compositions that include bcc crystallites may have the potential for combining high strength with tensile ductility. The brittle response that we measured for all alloyed thin films is likely due to extrinsic factors such as the presence of porosity. Nevertheless, measurements of the full suite of mechanical response over a large composition range are promising strategies to guide design of new materials with superior combinations of properties.
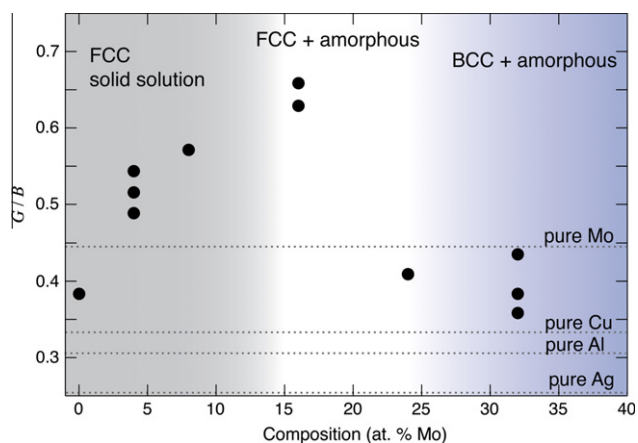

Fig. 10. Ratio of shear to bulk moduli (G/B) for Al–Mo thin films obtained from tensile testing. G/B ratios are also shown for several pure metals for comparison.

6. Conclusions

In summary, we have performed systematic tensile testing of submicron freestanding Al–Mo alloy sputtered thin films. The full mechanical behavior as a function of Mo content was measured, providing both elastic and plastic properties for a range of microstructures including solid solution and two-phase amorphous/crystalline mixtures. Full-field strain measurements during testing enabled direct determination of both Young's modulus and Poisson's ratio, allowing for calculation of all isotropic elastic constants. In addition, fracture strength was measured for all Mo compositions, providing insight to influence of Mo on thin film plasticity.

Based on the results and their interpretation presented herein, we draw the following conclusions:

- Our Al–Mo thin films synthesized via co-sputtering can consist of supersaturated solid solutions out to ∼10 at.% Mo, followed by a two-phase fcc/amorphous mixture at larger Mo content. Beyond ∼20 at.% Mo, ordered bcc domains within an amorphous matrix are observed.

- The isotropic elastic constants are very sensitive to the Mo content, particularly in the solid solution regime, with E, G and B increasing with the addition of Mo. Whereas B shows a linear relationship with Mo composition, indicative of adherence to Vegard's law, the elastic constants not mediated by hydrostatic stress states (E, G, and v) increase nonlinearly, suggesting the influence of changes to the electronic structure and the local atomic environment around Mo solutes in addition to internal strain. Poisson's ratio shows particular sensitivity to the amorphous or bcc phases as evidenced by a discontinuous change at ∼20 at.% Mo.

- Incorporation of Mo into Al thin films results in substantial strengthening, with the most potent effect resulting from solid solution strengthening (up to 5× higher fracture strength over that of pure Al thin films). Fleischer solid solution theory predicts the lower range of our measured strengths, whereas the combination of solid solution effects with a recently developed nanocrystalline solution pinning theory [59] better describe our experimental data. Calculation of the G/B ratio for our Al–Mo thin films implies the potential for tensile ductility at high Mo content, although the measured brittle behavior highlights the role of porosity in precluding large amounts of plastic flow.

Taken as a whole, our single step physical vapor deposition approach for synthesizing $Al_{1-x}Mo_x$ thin films produces a diverse set of microstructures over the Mo composition range studied, resulting in a large property space. Tailoring the elastic and plastic properties of such thin films could be used in dimensionally constrained applications such as MEMS/NEMS, energy storage and conversion, and corrosion-resistant and hard coatings.

References

[1] Weertman JR, Farkas D, Hemker K, Kung H, Mayo M, Mitra R, et al. MRS Bull 1999;24:44–50.

[2] Dao M, Lu L, Asaro R, Dehosson J, Ma E. Acta Mater 2007;55:4041–65.

[3] Kumar K, Van Swygenhoven H, Suresh S. Acta Mater 2003;51:5743–74.

[4] Koch CC. J Mater Sci 2007;42:1403–14.

[5] Hanlon T, Tabachnikova E, Suresh S. Int J Fatigue 2005;27:1147–58.

[6] Hanlon T. Scripta Mater 2003;49:675–80.

[7] Moser B, Hanlon T, Kumar KS, Suresh S. Scripta Mater 2006;54:1151–5.

[8] Padilla Ha, Boyce BL. Exp Mech 2009;50:5–23.

[9] Farhat ZN, Ding Y, Northwood DO, Alpas aT. Mater Sci Eng, A 1996;206:302–13.

[10] Jeong D, Gonzalez F, Palumbo G, Aust K, Erb U. Scripta Mater 2001;44:493–9.

[11] Rupert TJ, Schuh Ca. Acta Mater 2010;58:4137–48.

[12] Shen Y, Lu L, Dao M, Suresh S. Scripta Mater 2006;55:319–22.

[13] Chen M, Ma E, Hemker KJ, Sheng H, Wang Y, Cheng X. Science 2003;300:1275–7.

[14] Sanders PG, Rittner M, Kiedaisch E, Weertman JR, Kung H, Lu YC. Nanostruct Mater 1997;9:433–40.

[15] Hugo RC, Kung H, Weertman JR, Mitra R, Knapp jA, Follstaedt DM. Acta Mater 2003;51:1937–43.

[16] Kumar KS, Suresh S, Chisholm MF, Horton jA, Wang P. Acta Mater 2003;51:387–405.

[17] Budrovic Z, Van Swygenhoven H, Derlet PM, Van Petegem S, Schmitt B. Science 2004;304:273–6.

[18] Haslam aJ, Moldovan D, Yamakov V, Wolf D, Phillpot SR, Gleiter H. Acta Mater 2003;51:2097–112.

[19] Li L, Anderson PM, Lee M, Bitzek E, Derlet P, Van Swygenhoven H. Acta Mater 2009;57:812.

[20] Van Swygenhoven H, Derlet P. Phys Rev B 2001;64:1–9.

[21] Dalla Torre F, Van Swygenhoven H, Victoria M. Acta Mater 2002;50:3957–70.

[22] Van Swygenhoven H, Derlet PM, Frøseth aG. Acta Mater 2006;54:1975–83.

[23] Van Swygenhoven H, Derlet PM, Frøseth aG. Nat Mater 2004;3:399–403.

[24] Hasnaoui A, Van Swygenhoven H, Derlet P. Phys Rev B 2002;66:1–8.

[25] Huang X, Hansen N, Tsuji N. Science 2006;312:249–51.

[26] Koch CC. Nanostruct Mater 1997;9:13–22.

[27] Gianola DS, Van Petegem S, Legros M, Brandstetter S, Van Swygenhoven H, Hemker KJ. Acta Mater 2006;54:2253–63.

[28] Gianola DS, Warner DH, Molinari JF, Hemker KJ. Scripta Mater 2006;55:649–52.

[29] Rupert TJ, Gianola DS, Gan Y, Hemker KJ. Science 2009;326:1686–90.

[30] Meyers MA, Mishra A, Benson DJ. Prog Mater Sci 2006;51:427–556.

[31] Asaro RJ, Suresh S. Acta Mater 2005;53:3369–82.

[32] Van Petegem S, Brandstetter S, Van Swygenhoven H, Martin J-L. Appl Phys Lett 2006;89:073102.

[33] Yamakov V, Wolf D, Phillpot SR, Mukherjee AK, Gleiter H. Nat Mater 2002;1:45–8.

[34] Wolf D, Yamakov V, Phillpot SR, Mukherjee a, Gleiter H. Acta Mater 2005;53:1–40.

[35] Schiøtz J, Tolla FDD, Jacobsen KW. Nature 1998;391:561–3.

[36] Schiøtz J, Jacobsen KW. Science 2003;301:1357–9.

[37] Cahn JW, Taylor JE. Acta Mater 2004;52:4887–98.

[38] Cahn JW, Mishin Y, Suzuki A. Acta Mater 2006;54:4953–75.

[39] Legros M, Gianola DS, Hemker KJ. Acta Mater 2008;56:3380–93.

[40] Mompiou F, Legros M, Radetic T, Dahmen U, Gianola DS, Hemker KJ. Acta Mater 2012;60:2209–18.

[41] Gleiter H. Nanostruct Mater 1995;6:3–14.

[42] Weissmüller J. Nanostruct Mater 1993;3:261–72.

[43] Kirchheim R. Acta Mater 2002;50:413–9.

[44] Millett P, Selvam R, Saxena A. Acta Mater 2007;55:2329–36.

[45] Trelewicz J, Schuh C. Phys Rev B 2009;79:1–13.

[46] Cahn JW. Acta Metall 1962;10:789–98.

[47] Malow T, Koch C. Acta Mater 1997;45:2177–86.

[48] Michels A, Krill CE, Ehrhardt H, Birringer R, Wu DT. Acta Mater 1999;47:2143–52.

[49] Jin M, Minor AM, Stach EA, Morris JW. Acta Mater 2004;52:5381–7.

[50] Zhang K, Weertman JR, Eastman JA. Appl Phys Lett 2005;87:061921.

[51] Fan G, Fu L, Qiao D, Choo H, Liaw P, Browning N. Scripta Mater 2006;54:2137–41.

[52] Pan D, Kuwano S, Fujita T, Chen MW. Nano Lett 2007;7:2108–11.

[53] Brandstetter S, Zhang K, Escuadro A, Weertman JR, Van Swygenhoven H. Scripta Mater 2008;58:61–4.

[54] Gianola DS, Eberl C, Cheng XM, Hemker KJ. Adv Mater 2008;20:303–8.

[55] Gianola DS, Mendis BG, Cheng X, Hemker KJ. Mater Sci Eng, A 2008;483–484:637–40.

[56] Elsener A, Politano O, Derlet PM, Van Swygenhoven H. Acta Mater 2009;57:1988–2001.

[57] Schäfer J, Albe K. Scripta Mater 2011:10–2.

[58] Tang F, Gianola DS, Moody MP, Hemker KJ, Cairney JM. Acta Mater 2012;60:1038–47.

[59] Rupert TJ, Trenkle JC, Schuh CA. Acta Mater 2011;59:1619–31.

[60] Thompson C. Annu Rev Mater Sci 2000;30:159–90.

[61] Lee Z, Ophus C, Fischer LM, Nelson-Fitzpatrick N, Westra KL, Evoy S, et al. Nanotechnology 2006;17:3063–70.

[62] Ophus C, Luber EJ, Edelen M, Lee Z, Fischer LM, Evoy S, et al. Acta Mater 2009;57:4296–303.

[63] Almeida A, Carvalho F, Carvalho PA, Vilar R. Surf Coat Technol 2006;200:4782–90.

[64] Nii H, Miyagawa M, Matsuo Y, Sugie Y, Niibe M, Kinoshita H. Jpn J Appl Phys 2002;41:5338–41.

[65] Lin K, Ho Y, Ho J. Thin Solid Films 1995;263:85–91.

[66] Hoffmann H, Kücher P. Thin Solid Films 1987;146:155–64.

[67] Chow GM, Pattnaik a, Schlesinger TE, Cammarata RC, Twigg ME, Edelstein AS. J Mater Res 2011;6:737–43.

[68] Janik-Czachor M, Jaskiewicz A, Kedzierzawski P, Werner Z. Mater Sci Eng, A 2003;358:171–7.

[69] Wolowik A, Janikczachor M. Mater Sci Eng, A 1999;267:301–6.

[70] Principe EL, Shaw BA, Davis GD. Corrosion 2003;59:295–313.

[71] Crossland AC, Thompson GE, Wang J, Habazaki H, Shimizu K, Skeldon P, et al. J Electrochem Soc 1997;144:847.

[72] Gianola DS, Hemker KJ, Legros M, Sharpe WN. TMS Letters 2004;1:8–9.

[73] Gianola DS, Eberl C. JOM 2009;61:24–35.

[74] Sharpe WN, Pulskamp J, Gianola DS, Eberl C, Polcawich RG, Thompson RJ. Exp Mech 2007;47:649–58.

[75] Gianola DS, Sedlmayr A, Mönig R, Volkert Ca, Major RC, Cyrankowski E, Asif SAS, Warren OL, Kraft O. Rev Sci Instrum 2011;82:063901.

[76] Eberl C, Gianola DS, Thompson RJ, Sharpe WN, Hemker KJ. Matlab File Exchange 2006.

[77] Markmann J, Yamakov V, Weissmüller J. Scripta Mater 2008;59:15–8.

[78] Stukowski A, Markmann J, Weissmüller J, Albe K. Acta Mater 2009;57:1648–54.

[79] Walford LK. Phil Mag 1964;9:513–6.

[80] Chen I-W. J Am Ceram Soc 1986;4:189–94.

[81] Schuh C, Hufnagel T, Ramamurty U. Acta Mater 2007;55: 4067–109.
[82] Schuh CA, Nieh TG. J Mater Res 2011;19:46–57.
[83] Schuh CA, Nieh TG, Iwasaki H. Acta Mater 2003;51:431–43.
[84] Dudzinski N. J Inst Metals 1952;81:49–55.
[85] Taga A, Vitos L, Johansson B, Grimvall G. Phys Rev B 2005;71:1–9.
[86] Masuda-Jindo K, Terakura K. Phys Rev B 1989;39:7509–16.
[87] Matsumuro A, Murata K. J Mater Sci 1993;28.
[88] Hatch JE. Aluminum: properties and physical metallurgy. Materials Park, OH: ASM International; 1984.
[89] Van Horn K. Aluminum: properties, physical metallurgy and phase diagrams. Metals Park, OH: American Society for Metals; 1967.
[90] Haasen P. Physical metallurgy. Cambridge: Cambridge University Press; 1996.
[91] Zener C. Acta Crystallogr A 1949;2:163–6.
[92] Oliver WC, Pharr GM. J Mater Res 1992;7:1564–83.
[93] Fleischer RL. J Appl Phys 1962;33:3504.
[94] Scattergood R, Koch C, Murty K, Brenner D. Mater Sci Eng A 2008;493:3–11.
[95] Arzt E. Acta Mater 1998;46:5611–26.
[96] Cheng S, Spencer JA, Milligan WW. Acta Mater 2003;51 :4505–18.

[97] Donohue A, Spaepen F, Hoagland RG, Misra A. Appl Phys Lett 2007;91:241905.
[98] Wang Y, Li J, Hamza AV, Barbee TW. Proc Nat Acad Sci USA 2007;104:11155–60.
[99] Hofmann DC, Suh J-Y, Wiest A, Duan G, Lind M-L, Demetriou MD, et al. Nature 2008;451:1085–9.
[100] Greer JR, De Hosson JTM. Prog Mater Sci 2011;56:654–724.
[101] Kim J-Y, Jang D, Greer JR. Adv Funct Mater 2011;21:4550–4.
[102] Liu YH, Wang G, Wang RJ, Zhao DQ, Pan MX, Wang WH. Science 2007;315:1385–8.
[103] Conner RD, Johnson WL, Paton NE, Nix WD. J Appl Phys 2003;94:904.
[104] Conner RD, Li Y, Nix WD, Johnson WL. Acta Mater 2004;52:2429–34.
[105] Pugh SF. Phil Mag 1954;45:823–43.
[106] Hecker SS, Rohr DL, Stein DF. Metall Mater Trans 1978;9:481–8.
[107] Schroers J, Johnson W. Phys Rev Lett 2004;93:20–3.
[108] Chen M. Annu Rev Mater Res 2008;38:445–69.
[109] Lewandowski JJ, Wang WH, Greer AL. Philos Mag Lett 2005;85:77–87.
[110] Davis JR, editor. ASM specialty handbook: aluminum and aluminum alloys. Metals Park, OH: ASM International; 1993.